J. Appl. Cryst. (1989).22,321-333

Electronically Focused Time-of-Flight Powder Diffractometers at the Intense Pulsed Neutron Source

By J. D. JORGENSEN.* J. FABER JR.* J. M. CARPENTER.~ R. K. CRAWFORD,† J. R. HAUMANN,‡ R. L. HITTERMAN;* R. KLEB,* G. E. OSTROWSKI,~ F. J. ROTELLA† AND T. G. WORLTON†

Argonne National Laboratory, Argonne, IL 60439, USA

(Received 5 May 1988; *accepted* 1 *March* 1989)

Abstract

Two time-of-flight powder diffractometers have operated at the Intense Pulsed Neutron Source (IPNS) since August 1981. These instruments use dedicated microcomputers to focus time-of-flight events so that data from different detectors can be summed into a single histogram. Thus, large multidetector arrays can be employed at any scattering angle from 12 to 157°. This design permits data to be collected over a uniquely wide range of d spacings while maintaining high resolution and count rates. The performance of the two instruments is evaluated by analyzing data from a standard Al_2O_3 sample by the Rietveld method. These instruments provide the capability for moderate- to high-resolution measurements with the duration of a typical run being a few hours.

Introduction

The recent development of spallation pulsed neutron sources (Carpenter, Blewitt, Price & Werner, 1979; Carpenter, 1977; Brown, Carpenter, Jorgensen, Price & Kamitakahara, 1982; Windsor, 1981) has motivated a renewed interest in the time-of-flight (TOF) method of neutron powder diffraction because TOF techniques can be optimally used at pulsed sources (Jorgensen & Rotella, 1982). The pulsed neutron sources produce short intense bursts of neutrons at relatively low (10-100 Hz) repetition rates. This allows the design of TOF diffractometers which achieve high resolution by the use of a long incident flight path. Typical target/moderator designs exhibit a pulse width roughly proportional to wavelength, so that instrument resolution is nominally constant over the entire range of *d* spacings measured at a fixed scattering angle. High count rates are maintained by the use of multiple detector arrays which are 'focused' such that events from different detectors can be summed into the same histogram. These principles were all demonstrated by the operation of the high-resolution Powder diffractometer (HRPD) at Argonne's ZING-P prototype pulsed neutron source (Jorgensen & Rotella, 1982).

The HRPD clearly demonstrated the high and nearly constant resolution which could be achieved by the TOF technique at a pulsed neutron source but suffered from one important limitation. The geometrical time-focusing method employed in the HRPD did not allow large-area detector arrays to be used at scattering angles smaller than 90°. Even at 90°, the detector area was only about one-third of that used in back scattering (1600). This limitation is a result of the long incident and short scattered flight paths which characterize high-resolution TOF diffractometer designs. The condition for geometrical time focusing is (Carpenter, 1967)

$$l \sin\theta = \text{constant}, \qquad (1)$$

where l is the total flight-path length (incident plus scattered) and 2θ is the scattering angle (θ is the Bragg angle). Detectors placed on this locus will simultaneously receive neutrons scattered from the same plane spacing (d). However, since the scattered flight path is only a small fraction of ***1 (e.g. less*** than 10°/0 for the HRPD), geometrical time focusing becomes impossible to achieve for small θ. In this case, as θ varies above and below the nominal value for a detector array, the time-focused locus intersects the sample position at larger θ's, and extends to prohibitively large scattered flight paths at smaller θ's, thus making large detector areas impossible in practice. The shallow focusing locus for the 90° detectors of the HRPD is an example of this problem (Jorgensen & Rotella, 1982).

For state-of-the-art powder diffraction studies it is important to have available a wide range of scattering angles and to be able to achieve large detector areas at any angle. Unless a cold source or neutron guide tube is used, flux decreases rapidly with increasing wavelength. Additionally, long-wavelength neutrons can be subject to large extinction and absorption effects which can complicate data analysis. Thus, long d-spacing peaks are best measured at low scattering angles. This is particularly important for the study of large unit cells, unknown structures, and magnetic

* Materials Science Division.
† Intense Pulsed Neutron Source Division.
‡ Electronics Division.

0021 -8898 /89/040321 -13 S03.00

structures where form factors reduce scattered intensity at small d. Some special-environment diffraction problems require the largest possible detector area at a scattering angle dictated by the location of 'windows' in the sample cell. For example, high-pressure diffraction is best done at a scattering angle near 90° where collimation can be used to mask scattering from the pressure-cell walls (Jorgensen & Worlton, 1985). A number of design criteria for ancillary equipment to be used on TOF neutron powder diffractometers and examples of scientific applications have been discussed in previous reviews (Faber, 1984; Jorgensen, 1988).

Electronic time focusing

For these reasons, the design goal for the TOF powder diffractometers at IPNS was to achieve large focused detector areas over the entire range of angles covered by the instruments. Since this focusing cannot be done geometrically, on-line microcomputers are used to process signals from a large number of individual detectors before data histograms are constructed. Thus, histograms can be constructed based on a focused time, or pseudo-time, variable rather than actual TOF (Jorgensen & Faber, 1983; Faber & Hitterman, 1986).

If one uses the de Broglie relation,

$$\lambda = h/mv = ht/ml, \qquad (2)$$

Bragg's law can be written as

$$d = \lambda/(2 \sin \theta) = ht/(2ml \sin \theta), \qquad (3)$$

where **A is** wavelength, ***h is*** Planck's constant, ***m is*** neutron mass, v is neutron velocity, and *t* is the measured TOF. For an array of detectors at scattering angles $2\theta_i$ and path lengths l_i, neutrons scattered from planes of a particular spacing *d* are detected at the *ith* detector at time

$$t_i = (2md/h) l_i \sin \theta_i. \qquad (4)$$

This measured time can be processed to yield the desired pseudo-time, t*, which is the TOF that would have been measured for a detector at a reference position, l_0, θ_0, by multiplying by a constant:

$$t^* = t_i(l_0 \sin \theta_0)/(l_i \sin \theta_i). \qquad (5)$$

After making this calculation for each detector in an array, the data histogram can be constructed in terms of the pseudo-times, *t**. Thus, neutrons scattered from the same plane spacing, d, will be binned in the same channel of the data histogram. This method for electronically time focusing allows extended area detectors to be used at any scattering angle and also allows a given instrument to be properly focused on any incident flight-path length by simply reprogramming the focusing microcomputer.

Diffractometer design

Two powder diffractometers were constructed for use at IPNS (Jorgensen & Faber, 1983). The General Purpose (GPPD) and Special Environment (SEPD) Powder Diffractometers are of identical design but are situated on incident flight paths of different lengths and, thus, exhibit different performance. The GPPD has an incident flight path of 20 m and the SEPD one of 14 m. A schematic view of the instruments is shown in Fig. 1. The sample is at the center and is surrounded on both sides by detectors in the scattering plane at a constant radius of 1.5 m. Instrument shielding limits the available scattering angles to 12-157° on both the right- and left-hand sides. The detectors are 10 atm ^{3}He proportional counters 1.27 cm diameter by 38.1 cm long and are oriented perpendicular to the scattering plane.

The final instrument design was the result of Monte Carlo simulations which included the contributions of a finite moderator, sample and detector, as was done for the HRPD design (Jorgensen & Rotella, 1982). The goal was to achieve a single design suitable for use on incident flight paths from 10 to 30 m. As for the HRPD, the moderator surface has dimensions 10 x 10 cm. Thus, the (in-plane) angular divergence of the scattered beam (1.27 cm/150 cm) equals that of the incident beam for an incident flight path of about 12 m. For larger incident flight paths, the scattered beam divergence dominates and the overall geometrical resolution decreases slowly with increasing flight path. However, it is not advantageous to make the moderator surface larger (which would not degrade resolution significantly) because larger moderators cannot be as effectively coupled to the spallation target. Therefore, the expected gain in moderated neutron flux could not be realized in practice. Conversely, there is no point in making the

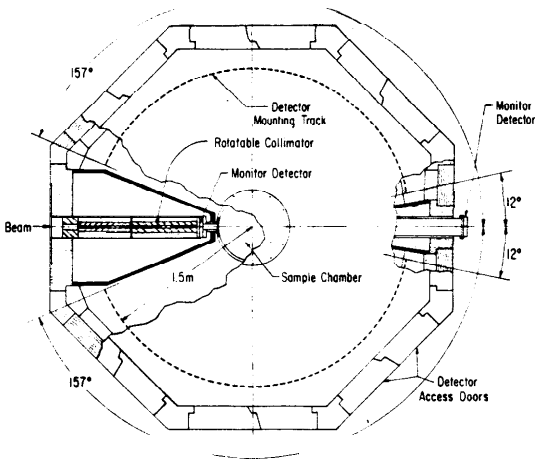

Fig. 1. Schematic diagram showing the overall layout of the General Purpose and Special Environment Powder Diffractometers.

Table l. ***Total geometrical resolution (FWHM) versus scattering angle for the GPPD and SEPD based on Monte Carlo calculations for a single detector (see text for details)***

GPPD Incident flight path: 20 m Scattered flight path: 1.5 m		SEPD Incident flight path: 14 m Scattered flight path: 1.5 m	
2θ (°)	Δ d/d	2θ (°)	Δ d/d
156	0.0014	155	0.0014
150	0.1016	150	0.0016
144	0.0017	145	0.0018
95	0.0040	95	0.0041
90	0.0043	90	0.0045
85	0.0047	85	0.0049
63	0.0072	63	0-0078
60	0.0077	60	0.0083
57	0.0083	57	0.0090
32	0.021	32	0.021
30	0.023	30	0.024
28	0.026	28	0.027
22	0.036	16	0.059
20	0.042	14	0.070
18	0.046	12	0.086

detector diameter smaller than the sample. Thus, some compromises are necessary in designing an instrument for use on a variety of flight paths.

The resolution of a TOF diffractometer is approximately given by

$$\Delta d/d = [(\Delta t/t)^2 + (\Delta\theta \cot\theta)^2 + (\Delta l/l)^2]^{1/2} \quad (6)$$

where Δd, Δt, $\Delta\theta$ and Δl are the uncertainties in the plane spacing, neutron TOF, Bragg angle and total flight-path length, respectively (Jorgensen & Rotella, 1982; Buras, Leciejewicz, Nite, Sosnowska, Sosnowska & Shapiro, 1964). The primary contribution to ***t is*** the width (in time) of the initial neutron pulse at the moderator. For an optimized instrument design, the time and geometrical contributions to the resolution are made equal by appropriate moderator design and choice of path lengths, detector size ***etc.*** Because of the cot θ term in (6), this optimization is possible at only one scattering angle.

In practice, it is difficult to evaluate (6) for three-dimensional moderators, samples and detectors. Moreover, for real systems the terms may not add as in (6) due to length–angle correlations. Thus, a computer simulation technique is used to evaluate and optimize the overall geometrical resolution. The computer code (***TOFDIF)*** selects a large number (~10^5) of paths connecting randomly chosen points in a two-dimensional moderator, two-dimensional sample and three-dimensional detector and evaluates the neutron time of flight for scattering from a constant ***d*** spacing. The geometrical resolution is then calculated from the distribution of these flight times.

Table 1 lists the total geometrical resolution ***versus*** scattering angle for the GPPD and the SEPD calculated as just described. The calculations assume a moderator 10 x 10 cm, a sample 1.2 x 5 cm, and a detector 1.27 x 1.27 x 38.1 cm. The angles chosen for" Table 1 are the centers and ends of the detector groups currently used in the two instruments. The longer flight path of the GPPD does not increase the geometrical resolution significantly since the angular divergence of the scattered path is the dominant term. The computer simulation calculations show that the contribution to the peak shape from the geometrical resolution is nearly Gaussian for 2θ larger than 60°, but is significantly asymmetric at smaller scattering angles. This asymmetry could be reduced significantly by using masks or shorter detectors at smaller scattering angles. Plots of the calculated distributions and a least-squares fit of a Gaussian to the distributions are shown in Fig. 2 for the SEPD at scattering angles of 150, 90, 60 and 30°. The resolution does vary somewhat within each detector group from one end to the other. This effect is more pronounced at small scattering angles. For example, the variation in resolution across the 10° wide detector group at 150° on the SEPD is ±8% while across the 4° wide detector group at 14° it is roughly ±20%. This variation in resolution across a detector group could result in an unusual peak shape, even if contributions from individual detectors were Gaussian. The resolutions for each detector could be made equal by varying the scattered flight path as a function of detector angle. In practice, however, previously developed peak-shape functions, which assume the geometrical contribution to be Gaussian (Von Dreele, Jorgensen & Windsor, 1982) appear to be suitable for Rietveld analysis of data from constant-radius focused detector arrays for scattering angles larger than 60°.

The source pulse width contribution to the resolution, ***At/t,*** depends on the moderator design. Typical moderator dimensions at IPNS are 10 x 10 cm by 5 cm thick. The pulse shape is determined by the time dependence of neutron thermalization and diffusion in the moderator and its width increases according to the moderator thickness. For most uses, the pulse width at thermal neutron energies is intentionally shortened by 'poisoning' the moderator with a thin sheet of neutron-absorbing material, the cross section of which varies with energy. When this is done, the entire moderator volume is active for moderation of neutrons above the energy at which the absorber becomes transparent, while the effective thickness of the moderator is reduced at thermal energies in order to achieve shorter pulses. Thus, the pulse width is controlled by the depth of the poisoning material.

The GPPD and SEPD view opposite faces of the same moderator. Two room-temperature moderator designs which have been used are reported here. (The current moderator is poisoned liquid methane and details of its performance will be discussed in a subsequent paper.) In both cases, the moderator material was polyethylene at about 323 K. The first moderator was poisoned in the center, ***i.e.*** a poisoning depth of

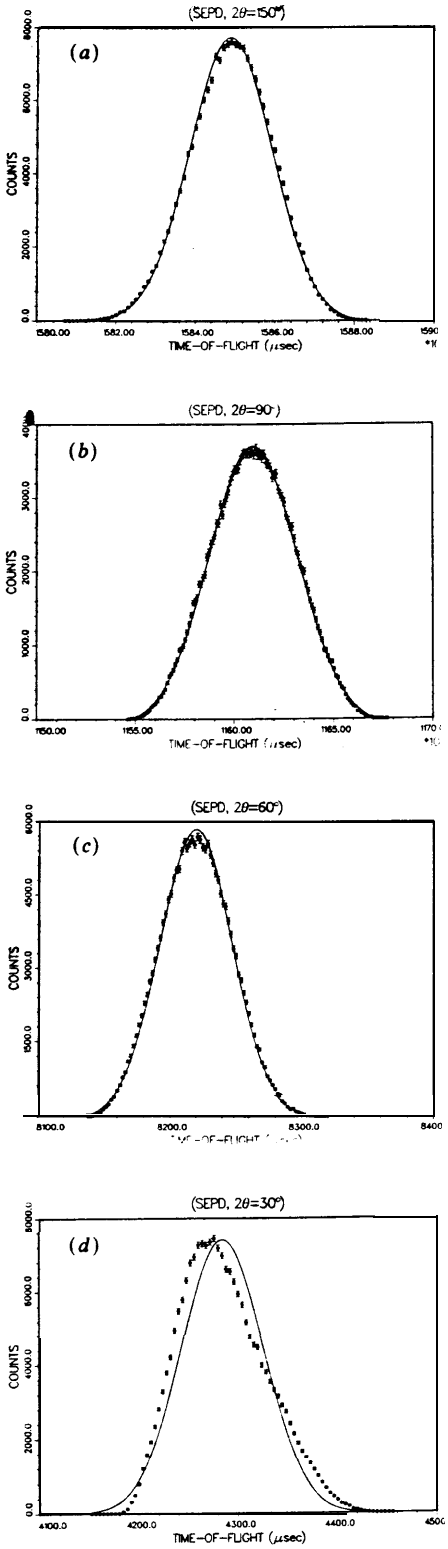

Fig. 2. Peak-shape distributions for the total geometrical resolution of the SEPD based on Monte Carlo calculations for a single detector at various scattering angles. The solid line is a least-squares fit Gaussian. ***(a)*** 2θ= 150°, (b) 2θ= 90°, (c) 2θ = 60°, (d) 2θ=30°.

2.5 cm from either surface, with a sheet of **O.5mm** thick cadmium. Later, the poisoning depth was reduced to 2.2 cm from either face by the use of two sheets of 0.5 mm thick cadmium. The source pulse width can be estimated by deconvoluting the constant (in terms of t/A)* geometrical resolution from the measured total instrument resolution or determined by measuring the peak shape using a single crystal in a time-focused arrangement (in which geometrical resolution is negligible). Measurements of neutron pulse shapes, by the latter method, for polyethylene moderators at IPNS are discussed in detail in a recent paper by Ikeda & Carpenter (1985).

Fig. 3 shows the pulse widths as a function of wavelength determined from GPPD data on the polyethylene moderator poisoned at 205 cm depth [which corresponds to the ***'H'*** moderator in the measurements of Ikeda & Carpenter (1985)], from SEPD data on the polyethylene moderator poisoned at 2.2 cm [which corresponds to the ***'F'*** moderator in the .

* For a given instrument, the pulse width can be expressed as **$\Delta t/t$ by using the relation $t = 252{\cdot}82\lambda l$, where t is the TOF in μs,** λ is the inferred wavelength in Å and *1* is the total path length (incident plus scattered) in m. Thus, a natural normalized time scale is t / λ; geometrical resolution contributions are constant in this variable.

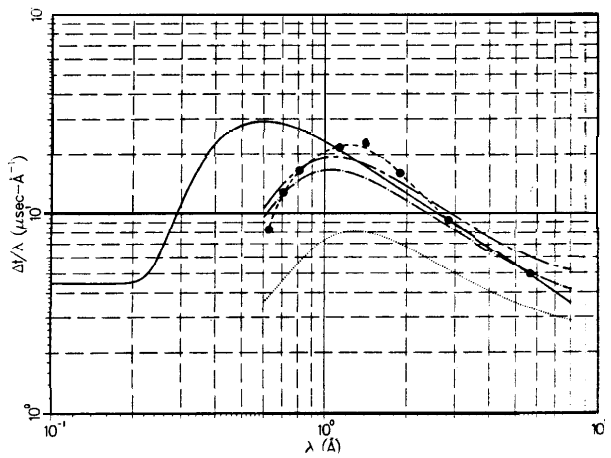

Fig. 3. The ratio of the standard deviation of the moderator pulse width, Δ ***t,*** to the wavelength, λ, as a function of the wavelength. (a) Dotted curve: net standard deviation determined (see text) by subtracting the geometric contribution to the variance from the variance of the Rietveld function fitted to HRPD data for 2θ= 160° detectors for a polyethylene moderator poisoned with 0.5 **mm** Cd, 1.27 cm beneath the viewed surface. (b) Chain-**dotted** curve: same, for SEPD data, 2θ= 150°, polyethylene moderator poisoned at 2.22 cm. (c) Chain-dashed curve: same, for GPPD data, 2θ= 150°, polyethylene moderator poisoned at 2.54 cm. (d) Filled circles: standard deviation determined from the time-of-flight Rietveld peak-shape function fitted to individual peaks in time-focused (geometric resolution negligible) single-crystal data for the moderator poisoned at 2.54 cm; the dashed curve is a guide to the eye. (e) Solid curve: standard deviation of the function of Ikeda & Carpenter, fitted to the single-crystal data for the 2.54 cm poisoned moderator.

measurements of Ikeda & Carpenter (1985)], and from HRPD data on the polyethylene **ZING-P *'A'*** moderator poisoned at 1.27 cm (Jorgensen & Rotella, 1982). For these curves ***(a, b,*** and c in Fig. 3 caption) the plotted function is the net standard deviation, ***At,*** determined from the variance of the peak-shape function in the Rietveld code in use at IPNS (Von Dreele, Jorgensen & Windsor, 1982; Rotella, 1988) and the calculated geometric contribution to the time distribution. The Rietveld peak-shape functions were determined by fitting diffraction peaks from a standard silicon powder sample, ***via*** the TOF Rietveld method, using the peak-shape function and the *d* dependence* of α, β and σ given by equations (10), (17), (18) and (19) of Von Dreele, Jorgensen & Windsor (1982). The geometric contribution to the time variance was that calculated by a Monte Carlo simulation of the instrument. The net standard deviation was calculated according to

$$\Delta t = (1/\alpha^2 + 1/\beta^2 + \sigma^2_{\text{geom}})^{1/2}, \qquad (7)$$

where $1/\alpha^2 + 1/\beta^2 + \sigma^2$ is the variance of the peak-shape function in the Rietveld code. Comparison of curves ***(a), (b)*** and (c) in Fig. 3 reveals the improvement in resolution that can be achieved by using poisoning to reduce the pulse width.

The subtraction of the geometric contribution to the variance, (7), is rigorously defensible, but the result is accurate only insofar as the variance of the Rietveld-fitted peak-shape function is accurate. This procedure represents a rather stringent test of the peak-shape fitting used currently in TOF Rietveld analysis. Herein lie some subtle points that are explored below.

Also shown in Fig. 3 are the standard deviations of the Ikeda-Carpenter functions computed directly from their fitted function (which gives a quite accurate representation of the peak shapes) and of those derived from the peak-shape function used in TOF Rietveld analysis, fitted to the ***data*** of Ikeda & Carpenter (but ***without*** imposing the ***d*** dependence on α, β and σ as above). These relate to, and should be compared with, the IPNS ***'H'*** moderator results (chain-dashed curve in Fig. 3). The Rietveld-fitted results correspond reasonably well to those for the ***'H'*** moderator, but there remain substantial discrepancies which we attribute to ***(a)*** the form of the peak-shape function and the imposed ***d*** dependence of the parameters α, β and σ (Von Dreele, Jorgensen & Windsor, 1982), which seem to smooth out the net standard deviation as a function of wavelength, and (b) the procedure of least-squares fitting of the peak shapes, which does not preserve the variance of the fitted data if the peak-shape model is not an accurate description of the peak shapes. This latter point is illustrated by the considerable discrepancy between the standard deviation of Ikeda-Carpenter-fitted functions and that of the Rietveld-fitted functions, which is being underestimated at short wavelengths.

This test of (6) reveals mostly that the 'tail', described by β in the peak-shape function, is not accurately represented by the fitted function; meanwhile, the variance depends strongly on the value of β This is the reason that the present testis so stringent. However, the test does not necessarily impugn the accuracy of peak intensity determination in the current TOF Rietveld code.

The curves in Fig. 3 illustrate an unusual wavelength dependence of the moderator pulse width. Since the geometric resolution contribution is constant, this wavelength dependence appears in the overall resolution. The Rietveld-fitted $\Delta t/\lambda$ ***versus*** λ curves illustrate that the analytical peak-shape function used currently in TOF Rietveld analysis (Von Dreele, Jorgensen & Windsor, 1982) differs markedly from the actual resolution functions at short wavelengths, which are not used customarily when analyzing data. This problem limits the minimum ***d*** spacing that can be refined successfully, even though data often extend to very small ***d.*** Peak intensities are not ***necessarily*** misrepresented by functions which do not accurately represent the observed peak shape, but unless peak shapes are represented accurately, it cannot be guaranteed that the intensities of unresolved peaks are determined properly by Rietveld analysis. Future efforts to improve Rietveld refinement of pulsed neutron source data must include a better model of the wavelength dependence of the peak-shape function based on correct physics. The direct measurements of moderator pulse width by Ikeda & Carpenter (1985) and the functions they have presented to fit their data should make this possible.

The general features of the moderator performance are clear from Fig. 3. Shallow poisoning improves resolution at all wavelengths. Also, the wavelength dependence of ***t*** is reduced as poisoning depth is decreased. However, these improvements in resolution are accompanied by a corresponding loss of thermal flux. The moderators poisoned at 2.5 and 1.27 cm differ in integrated thermal flux by a factor of 2.5 (Jorgensen & Rotella, 1982; Carpenter, Price & Swanson, 1978; Graham & Carpenter, 1972). For this reason, most moderator designs represent a compromise between resolution and neutron flux.

The design philosophy for the GPPD and SEPD can be seen by combining [according to (6)] the

* The emission time distribution and thus the width of Δt [(7)] for a moderator depends, strictly speaking, on wavelength A only, and not upon plane spacing ***d,*** the working variable in TOF Rietveld analysis. At fixed Bragg angle, however, one can speak interchangeably of ***d*** dependence or of λ dependence, since they are related by a constant factor according to Bragg's law. The observed peaks are broadened in TOF, t, which is the variable dispersed in the instrument. However, locally in the neighborhood of a peak, one can speak interchangeably of *t* and ***d,*** since these are (locally and at fixed Bragg angle) related by a constant factor.

geometrical resolution given in Table 1 and the pulse-width resolutions shown in Fig. 3. If both of these contributions to resolution were independent of wavelength, there would be a single scattering angle for each instrument where the two contributions were equal; this is the scattering angle at which the instrument is optimized. For the moderators used, ***t/t is*** somewhat wavelength dependent, as shown in Fig. 3. However, the approximate angle at which each instrument is optimized is evident. The pulse-width resolution for the GPPD closely matches the geometrical resolution in back scattering (150°), while that for the SEPD closely matches the geometrical resolution at 90°. In this way, the SEPD is optimized for special-sample-environment diffraction where the 90° scattering angle is an advantage for achieving the best possible collimation to eliminate unwanted scattering from the sample environment (e.g. pressure cells, heat shields etc.). The GPPD is optimized in back scattering for general-purpose high-resolution diffraction (Faber & Hitterman, 1986). For the present path lengths of the SEPD and GPPD the optimization is not perfect. However, it should be remembered that the design goal was a single instrument configuration suitable for use on incident flight paths from 10 to 30 m. Thus, true optimization in back scattering (150°) does not occur until the 30 m path length is reached.

Mechanical specifications

As shown in Fig. 1, the diffractometers are constructed as integral units containing the final collimators, sample chamber and detectors. The instrument shielding is incorporated into the mechanical support structure. The top and bottom octagonal sections consist of 10 cm of borax and 15 cm of polyethylene sandwiched in steel. Hinged doors along the sides of the instrument provide access to the detectors. These doors also consist of 10 cm of borax and 15 cm of polyethylene in a steel shell. In all cases, the borax faces the inside of the instrument. The complete instrument is octagonal, 3.8 m across and 1.2 m high and weighs approximately 20000 kg (22 ton), and is supported by eight steel legs. Final collimation of the incident beam is done inside the instrument just ahead of the sample chamber. The beam first passes through a 48 cm long steel collimator, fixed in position, with an aperture of 7.6 x 2.5 cm. The final collimator is in two pieces, each 22.9 cm long, inserted in a 60.6 cm diameter steel disc. The disc rotates around a horizontal axis perpendicular to the beam to allow selection of three different beam sizes according to the collimator inserts which are installed. The collimator inserts are cast from a boron carbide-epoxy resin mixture with a tapered aperture. The standard beam size is 5.08 x 1.27 cm (umbra) measured at the sample position. Smaller beam sizes are provided for use with special sample environments. The rotating collimator is operated by a crank inserted through a hole in the shielding from the top of the instrument. The shielding around the collimator assembly is wedge shaped with an included angle of 44° and is constructed from a 6.3 mm thick steel shell which encloses the shielding materials. One-inch-thick boron carbide is used to line the surfaces which face the detectors. The remaining volume of the wedge is filled with polyethylene.

The sample chamber is an aluminium tank 66 cm OD and 130 cm long with 2.54 cm thick walls, extending outside the instrument shielding at both the top and bottom. The chamber is carefully aligned with respect to the beam such that the center of the sample is 61 cm directly below (perpendicular to) the center of the top cover to an accuracy of about 0.3 mm. A variety of special-sample-environment equipment, including furnaces, closed-cycle helium refrigerators, cryostats and pressure cells, can be supported from suitable top covers. The cover plate and whatever equipment is supported from it is handled by a 1/2 ton capacity air-driven hoist on an overhead jib-boom crane mounted on the top surface of the instrument.

The incident neutron beam enters the sample chamber through a 0.5 mm thick aluminium window which is located within the collimator shielding wedge where it is not viewed by any of the detectors in the scattered flight path. The exit window (0.8 mm thick aluminium) is located outside the instrument at the end of a 15 cm diameter pipe connected to the chamber. The sample chamber is evacuated through this exit pipe or, alternately, through the bottom of the sample chamber by mechanical, oil diffusion or cryo pumps. The wall of the sample chamber has been thinned to 3.2 mm over a 17.8 cm high region extending from 8 to 159° on both sides of the beam to reduce losses and multiple scattering in the scattered beam path. Low-efficiency (10^{-4}) flat-plate BF_3 monitor detectors are located immediately outside the entrance and exit windows in order to measure the incident and transmitted beams.

Detectors are located in the scattering plane at a constant radius of 1.5 ± 0.0003 m from the sample position. The detectors are 10 atm ^{3}He proportional counters 1.27 cm diameter and 38.1 cm active length and are supported in mounting frames in groups of up to 20 per frame. The frames clamp to accurately aligned curved rails at the top and bottom. Detectors can be easily repositioned to meet the requirements of a given experiment. However, in practice, detector positioning and grouping remain constant for long periods of time in order to avoid the need for frequent recalibration of the instruments. The most commonly used detector configurations for the GPPD and SEPD are given in Table 2. The detector chamber is dehumidified to minimize electrical noise due to corona discharge. Reliable operation is achieved for relative humidity levels under 40% at 299 K.

Table 2. ***Typical performance parameters for the GPPD and SEPD at IPNS (June 1984)***

The resolutions are quoted for $\lambda = 3$ Å. Detectors are equally divided between the right and left sides except at 30, 20 and 14°.

GPPD
Incident flight path: 20 m, scattered flight path: 1·5 m
Thermal flux on sample: $7{\cdot}5 \times 10^9$ neutrons m^{-2} s^{-1}

Mean 2θ (°)	Number of detectors	Detector area (srd)	d_{min} (Å)	d_{max} (Å)	$\Delta d/d$ (FWHM)
150	48	0·103	0·41	2·86	0·0029
90	40	0·086	0·57	3·90	0·0049
60	24	0·052	0·80	5·52	0·0080
30	8	0·017	1·55	10·66	0·023
20	8	0·017	2·30	15·89	0·04

SEPD
Incident flight path: 14 m, scattered flight path: 1·5 m
Thermal flux on sample: $1{\cdot}5 \times 10^{10}$ neutrons m^{-2} s^{-1}

Mean 2θ (°)	Number of detectors	Detector area (srd)	d_{min} (Å)	d_{max} (Å)	$\Delta d/d$ (FWHM)
150	40	0·086	0·41	3·96	0·0034
90	40	0·086	0·57	5·41	0·0054
60	24	0·052	0·80	7·65	0·0088
30	8	0·017	1·55	14·79	0·024
14	8	0·017	3·28	30·36	0·07

During the initial operation of the instruments it was determined that a significant contribution to the background came from neutrons multiply scattered from the sample, the thick regions of the aluminium sample chamber, and the steel surfaces of the detector chamber. For this reason, 1.3 cm thick plates of boron carbide-epoxy resin mixture (less than 10°/0 epoxy by weight) were used to construct rectangular cross section truncated pyramidal shielding cones extending from each detector group to the surface of the sample chamber. A similar plate was placed directly behind each detector group. This additional shielding lowered the background by roughly a factor of two for most experiments. The elimination of these sample-dependent backgrounds is especially important for accurate measurements to high momentum transfers on amorphous solids and liquids.

Data acquisition system

A block diagram of the data acquisition system is shown in Fig. 4. A preamp is mounted directly on the connector of each detector. The resulting amplified signals (about 1 volt peak) travel through long (~50 m) coaxial cables (RG-174U) to the data acquisition system (Crawford, Daly, Haumann, Hitterman, Morgan, Ostrowski & Worlton, 1981; Haumann, Daly, Worlton & Crawford, 1982). Discrimination and time encoding occur in modules in a CAMAC system with eight detector inputs per module. Up to 20 data discriminator modules can be mounted in one CAMAC crate, and up to six crates can be daisy chained together. All of the modules are connected to a single 8 MHz master clock. Whenever one of the inputs receives an analog pulse within the discriminator window, a 20-bit time word (125 ns resolution) is combined with 3 bits of input identification and loaded into a first-in-first-out (FIFO) buffer in the module. Each FIFO buffer can store up to sixteen 24-bit words (the 24th bit is used to indicate FIFO overflow). A polling module, which communicates though the CAMAC dataway, scans the FIFO buffers and identifies those which are over half full. The 8-bit addresses of the FIFO buffers to be read are passed to a Multibus (Intel Corp., Santa Clara, CA) system where, in the initial implementation, a single 28001 microcomputer (Zilog Inc., Cupertino, CA) reads the data from the buffer and stores it in a circular raw data buffer in Multibus memory. Each event is, then, represented by a 32-bit word containing 20 bits of time information, 11 bits of detector identification, and one overflow bit.

When not busy retrieving raw data, the 28001 microcomputer processes the 32-bit raw data words in memory to construct data histograms. If time-focusing of the data is desired, the operation described by (5) is performed. The multiplicative constants for each detector,

$$(l_0 \sin \theta_0)/(l_i \sin \theta_i), \tag{8}$$

are calculated by a PDP 1l/34A computer (Digital Equipment Corp., Maynard, MA) during the setup of the run and are stored in a look-up table in Multibus memory. The reference detector position, defined by l_0 and θ_0, is normally taken as the center of a group so that the correction factors (8) are distributed around unity. Integer multiplication is employed to

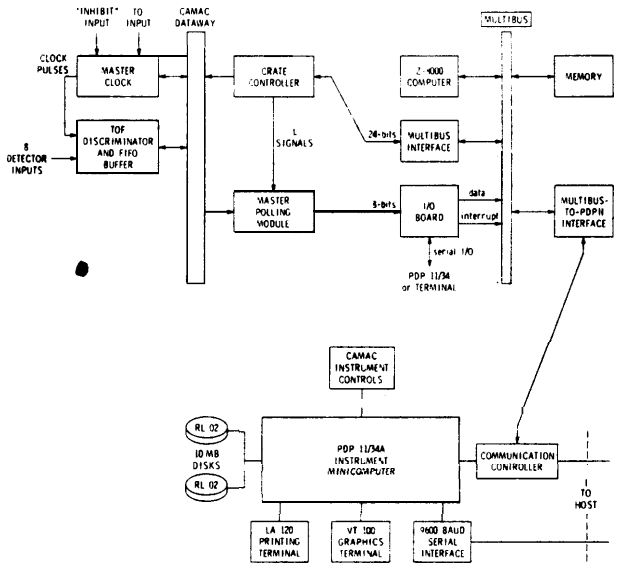

Fig. 4. Block diagram of the data acquisition system for the SEPD and GPPD.

achieve high processing rates. With focusing, the maximum average data rate of a single Z8001 is about 3000 Hz. The data collection software is written so that the same event can be processed into more than one histogram; ***i.e.*** it is possible to construct multiple histograms, focused or grouped in different ways, from the same data within the constraint of an overall 3000 Hz average data processing rate. After the pseudo-times t^* defined in (7) are calculated, the data are histogrammed into larger time channels (typically 5 to 50 μs) which match the instrument resolution. The use of a 125 ns clock period minimizes the propagation of errors during the focusing and histogramming calculations.

System dead time for an individual detector is 1-2 μs, arising from the detector pulse shape and the desire for both lower- and upper-level discrimination. All inputs are independent, so simultaneous pulses from two or more detectors will be encoded properly. The use of buffers, both in the discriminator modules and in the Multibus memory, allows high instantaneous data rates with no additional dead time due to the electronics, even though the time-averaged histogramming rate is only 3000 Hz. If the time-averaged data rate exceeds 3000 Hz for an appreciable period, the buffers saturate and the system stops, as this is a fundamental limit.

To alleviate this data rate problem, the Z8001 microcomputer on each instrument has recently been replaced with a system of one to four N32016 microcomputers (National Semiconductor Corp., Santa Clara, CA) operating in parallel. The same time-focusing and histogramming algorithms used with the Z8001 are still in use on the new systems, but the improved hardware configuration will now handle time-averaged data rates ranging from 7000 Hz for a one-microcomputer system to 30000 Hz for a four-microcomputer system. This effectively removes any limitations on time-averaged data rates for all envisaged samples at present IPNS source flux levels.

The PDP 1l/34A computer controls input and output functions of the data acquisition system and programs the Z8001 (or N32016) microcomputer. One RL02 10 Mbyte hard disk stores operating programs; a second disk is for long-term data storage. The PDP 1l/34A also controls a graphics display, which permits the user to view in real time the data in any of the detector groups using units relevant to the problem (channel, time-of-flight, *d* spacing, or momentum transfer).

[n addition, the PDP 1l/34A computer is interfaced to various sample environment control/monitoring features (sample temperature, sample changer position), permitting automated cycling through a number of samples and/or sample temperatures.

An alternative to the 'on-the-fly' time-focusing technique used here would be to histogram the data from each detector individually and then group detectors in the analysis stage. In this case, very narrow channels (less than 1 μs) should be used for the initial histograms in order to prevent significant peak shape and position distortions during the focusing and grouping process. This would in turn require large data sets to be stored and manipulated (30 000 μs range at 1 μs/channel = 30000 channels; 30000 channels/detector x 120 detectors = 3.6 million channels per data set). For these reasons, the present 'on-the-fly' focusing technique was adopted. With this approach, and the use of a 125 ns clock period, any peak shape and position distortions due to the focusing and grouping process are negligible at the present resolution levels. Alternative data binning schemes that are optimized for time-resolved studies have also been discussed (Faber, 1984) and can be implemented on the GPPD and SEPD if desired.

Instrument performance

The thermal neutron fluxes per unit proton current at the sample positions of the GPPD and SEPD have been estimated from gold foil activation measurements, Monte Carlo calculations of the target/moderator system, and comparison with HRPD performance for standard samples. For the original moderator, poisoned at a depth of 2.5 cm, and a proton energy of 450 MeV the measured (gold foil) thermal flux at the sample position per unit proton current is 5×10^8 neutrons $m^{-2} s^{-1} \mu A^{-1}$ for the GPPD and 1×10^9 neutrons $m^{-2} s^{-1} \mu A^{-1}$ for the SEPD. This measured flux is higher than predicted by Monte Carlo calculations by a factor of two for both instruments. The unexpected high flux is confirmed by data rates for standard samples. The cause of this discrepancy in the calculations is not known.

The measured resolutions ***versus d*** spacing for various scattering angles on the GPPD and SEPD are shown in Fig. 5. These curves are obtained by refining the coefficients of the peak-shape function in a Rietveld refinement (Von Dreele, Jorgensen & Windsor, 1982) for data from a standard sample (e.g. silicon). Since the geometrical resolution becomes more dominant, the wavelength dependence of the pulse width is masked and the overall resolution is more constant for smaller scattering angles. Resolution is not plotted for scattering angles smaller than 60° but can be easily estimated from Table 1 and Fig. 3.

The performance parameters of both instruments are summarized in Table 2. For powder diffraction experiments, d_{min} corresponds to a neutron wavelength of 0.8 Å because of limitations in data analysis (see below), not data collection. At the present time, the peak shapes and incident neutron spectrum are not sufficiently well parameterized by analytic functions to allow accurate Rietveld refinements at wavelengths shorter than this (Von Dreele, Jorgensen & Windsor, 1982). It should be noted, however, that

much shorter wavelengths are useable for diffraction from amorphous systems and liquids where closed-form expressions for the resolution and incident flux are not required for analysis. Present experience with diffraction studies of amorphous systems indicates that wavelengths as short as 0.2 Å can be used in that case. The maximum useable wavelength is limited by frame overlap, ***i.e.*** the situation where the next pulse leaves the moderator before longer-wavelength neutrons from the current pulse can be detected. IPNS operates at a repetition rate of 30 Hz. For the GPPD, with a total path length of 21.5 m, the maximum useable wavelength before frame overlap is 6.1 Å. For the SEPD, with a total path length of 15.5 m, it is 8.5 Å. When electronic time focusing is employed, these numbers must be reduced by up to 10% since an extended detector group scans a window of wavelengths in order to construct a focused histogram. The d_{max}'s listed in Table 2 are those actually used on the instruments and include considerations for both frame overlap and focusing.

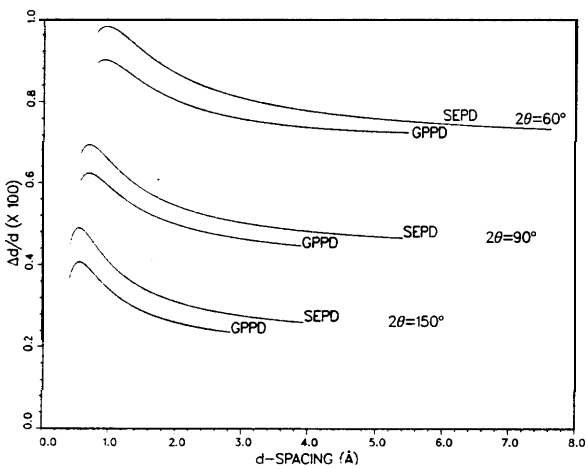

Fig. 5. Measured total resolution, $\Delta d/d$ (full width at half maximum) versus d spacing for various scattering angles on the GPPD and SEPD. These curves are for the moderator poisoned at a depth of 2.22 cm.

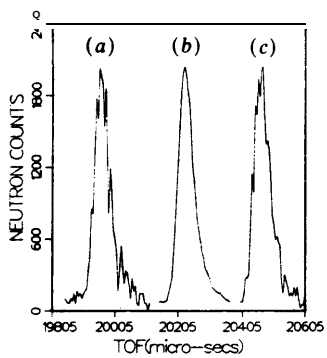

Fig. **6.** Raw data for a Bragg peak as measured by individual detectors and by the focused sum of an extended detector group. The individual detectors, (a) and (c), are the end members of the 150° detector group in the GPPD, plotted as a function of the measured TOF, and are at 145 and 155° respectively. At ***(b)*** is the focused sum for the entire group, focused to a reference angle of 150°.

Table 3. *Typical calibration constants for the GPPD and SEPD determined by Rietveld refinement of silicon data*

	C (μs Å^{-1})	A (μs Å^{-2})	Z (μs)
GPPD: 150°	10504·925	−4·21	−13·69
90°	7697·944	−3·00	−17·57
60°	5456·580	−1·69	−22·12
30°	2808·440	0	0
SEPD: 150°	7569·579	−2·66	−9·92
90°	5592·286	−2·44	−13·65
60°	3938·234	−1·81	−17·06
30°	2028·465	0	0

The electronic focusing hardware and software have been tested by comparing unfocused data from single detectors within a group with the focused sum for the group (Faber, 1984). Fig. 6 shows raw data for a Bragg peak measured by individual detectors at the ends of a group and for the focused sum of the group. The resolutions agree with predictions and the focused peak is not additionally broadened. Thus, the electronic focusing hardware and software function correctly.

Results for standard samples

Standard samples have been used to calibrate the instruments and to evaluate their performance. Silicon powder is typically used for instrument calibration. The silicon lattice constant is assumed to be 5.4309 Å. Rietveld refinement of silicon data is performed to establish the constants C, A and Z which relate the measured time of flight to the d spacing in the relation

$$t = Cd + Ad^2 + Z \qquad (9)$$

for each scattering angle. Typical values for these calibration constants are given in Table 3. Silicon is not useful as a calibrant for angles below 60° because of its small unit cell. Thus, the constants listed in Table 3 for the smaller scattering angles are approximated from data for other samples. Values for the six coefficients which define the wavelength dependence of the peak shape (Von Dreele, Jorgensen& Windsor, 1982) are also obtained from the silicon refinements. It is these coefficients which are used to plot the resolution curves of Fig. 5.

Since alumina, $A1_2O_3$, has been studied on many powder diffractometers for the purpose of comparing instrument performance (Andresen & Sabine, 1977; Hewat & Bailey, 1976; Jorgensen & Rotella, 1982; Tompson, Mildner, Mehregany, Sudol, Berliner & Yelon, 1984), data for $A1_2O_3$ have been used to evaluate the performance of the GPPD and SEPD. The

Table 4. *Structural parameters for Al_2O_3 determined by Rietveld refinement of data from the* **150** *and 90" detector groups of the GPPD and SEPD*

Parameters are expressed in the hexagonal setting of space group $R\bar{3}c$. Numbers in parentheses are standard deviations of the last significant digit. Anisotropic temperature factors are of the form

$$\exp[-2\pi^2(h^2a_0^{*2}U_{11}+k^2b_0^{*2}U_{22}+l^2c_0^{*2}U_{33}+2hka_0^*b_0^*U_{12}+2hla_0^*c_0^*U_{13}+2klb_0^*c_0^*U_{23})].$$

	GPPD		SEPD	
	150°	90°	150°	90°
a_0 (Å)	4·7580 (1)	4·7573 (1)	4·7579 (1)	4·7575 (1)
c_0 (Å)	12·9935 (1)	12·9913 (2)	12·9929 (1)	12·9914 (2)
V_0 (Å^3)	254·740 (2)	254·629 (3)	254·718 (2)	254·645 (4)
z(Al)	0·35212 (4)	0·35238 (6)	0·35215 (5)	0·35228 (6)
x(O)	0·30626 (4)	0·30628 (7)	0·30630 (5)	0·30619 (7)
U_{11}(Al)	0·00208 (11)	0·00217 (23)	0·00193 (13)	0·00182 (24)
U_{33}(Al)	0·00291 (17)	0·00366 (38)	0·00299 (17)	0·00280 (42)
U_{11}(O)	0·00258 (10)	0·00279 (18)	0·00245 (11)	0·00229 (19)
U_{33}(O)	0·00333 (9)	0·00369 (16)	0·00316 (10)	0·00300 (16)
U_{12}(O)	0·00142 (14)	0·00141 (30)	0·00138 (15)	0·00129 (29)
U_{13}(O)	−0·00052 (7)	−0·00062 (13)	−0·00041 (8)	−0·00077 (15)
d_{min} (Å)	0·41	0·55	0·41	0·55
d_{max} (Å)	2·55	3·48	2·55	3·48
Number of reflections	405	175	408	175
R_{F^2}	0·0214	0·0174	0·0139	0·0155
R_{wp}	0·0406	0·0384	0·0360	0·0369
R_{exp}	0·0166	0·0122	0·0171	0·0132
S/N 113 reflections (d = 2·084 Å)	242	164	246	135

R values are calculated from the following expressions:

$$R_{F^2} = \sum_j |I_j(\text{obs.}) - I_j(\text{calc.})| / \sum_j I_j(\text{obs.})|,$$

$$R_{wp} = \left\{ \sum_i w_i[Y_i(\text{obs.}) - Y_i(\text{calc.})]^2 / \sum_i w_i[Y_i(\text{obs.})]^2 \right\}^{1/2},$$

$$R_{exp} = (N - V) / \sum_i w_i[Y_i(\text{obs.})]^2,$$

where I_j(obs.) and I_j(calc.) are the observed and calculated integrated intensities of the *jth* Bragg reflection; Y_i(obs.), Y_i(calc.) and $w_i[= 1/Y_i(\text{obs.})]$ are the observed counts, calculated counts and statistical weight, respectively, for the *ith* data point; N is the number of data points; and ***V is*** the number of variables.

sample used for the data presented here is one standard sintered pellet 13·5 mm diameter and 16 mm long distributed by Andresen & Sabine (1977) for comparing powder instruments. Data have been refined for the 150 and 90° detector groups on both instruments using the Rietveld code currently in use at IPNS (Von Dreele, Jorgensen & Windsor, 1982; Rotella, 1988). The results are summarized in Table 4. Raw data and the refined profiles for the GPPD 150° refinement and the SEPD 90° refinement are shown in Figs. 7 and 8. In all cases, the data were refined over the same range of neutron wavelengths, 0·8 to 5·0 Å. As is clear in Figs. 7 and 8, the useful data extend to even smaller d spacings. However, the refinement range was not extended because of the lack of accurate analytical descriptions of the peak shape and incident intensity *versus* wavelength at wavelengths smaller than 0·8 Å.

For the refinements, the product of the incident neutron spectrum and the detector efficiency has been determined from the incoherent scattering from a 6·4 mm diameter vanadium rod. The raw vanadium data are corrected for absorption and multiple scattering. The function described by Von Dreele, Jorgensen & Windsor (1982) is then least-squares fitted to the corrected vanadium data to obtain a set of coefficients which are used as input to the Rietveld refinement.

By comparing the refined values of the structural parameters and their standard deviations for the four refinements reported in Table 4, some useful conclusions can be drawn about the effects of the improved resolution and extended small d spacing data range that can be obtained in back scattering. Additionally, the results of the four refinements illustrate some of the systematic errors that are common to time-of-flight neutron diffraction.

For the same scattering angle, both instruments give the same unit-cell parameters within a precision which is limited by the accuracy of sample alignment. However, for a given instrument, the 150 and 90° refinements yield systematically different values for a_0 and c_0. This systematic difference in cell parameters as a function of scattering angle is easily explained as a small shift in the effective sample

position which results because the total cross section of the $A1_20_3$ sample is larger than that of the silicon calibration sample. The fractional error in cell parameters due to this effect is equal to the fractional error in the measured time of flight, which is given by

$$t/t = (x/2l_2) \cot \theta + x/l, \qquad (10)$$

where l is the total flight-path length, l_2 is the scattered flight path length, 2θ is the scattering angle and Δx is the shift in the effective sample position along the direction of the incident neutron beam. For the Al_20_3 results in Table 4, the difference between the 150 and 90° cell parameters can be inserted into (10) yielding a value for x of − 0.4 mm (where the negative sign indicates that the shift is toward the neutron source, as expected from the larger cross section of $A1_20_3$). The error due to this effect is smallest in back scattering, owing to the cot θ term in (10). If a precise quantitative determination of cell parameters is required, the sample cross section can be used to calculate the effective sample position and the resulting change in calibration constants at each scattering angle.

The scatter in refined values for atom positions and anisotropic temperature factors appears to exceed the statistical uncertainties for some parameters, suggesting that small systematic errors, not included in the refinement model, are present. The total deviations are, however, quite small. For example, the total spread in the refined values for z(Al) is equivalent to 0.003 Å. Possible causes of these errors include texture effects in the sintered sample and errors in modeling the peak shape, the incident spectrum *versus* wavelength, and wavelength-dependent corrections to intensity such as extinction and absorption. Systematic errors which have a monotonic wavelength dependence would be expected to manifest themselves primarily in the temperature factors. Evidence for such errors appears to be present in the temperature factors reported in Table 4; *i.e.* the temperature factors generally seem to scale together for a given instrument and scattering angle. This effect is most clearly evidenced by the U_{ij}'s for the 90° data from the SEPD, which seem to fall uniformly slightly below the values from the other refinements. In

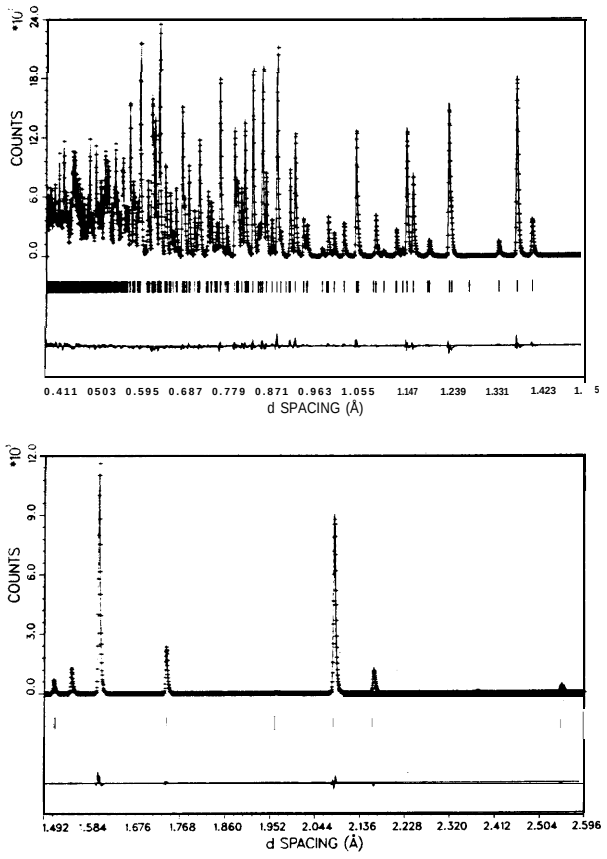

Fig. 7. Raw data (+) and calculated diffraction profile (solid line) from Rietveld refinement of Al_20_3 data collected on the 150° detector group of the GPPD. Tick marks below the profile indicate the positions of all allowed Bragg reflections used in the calculation. A difference curve, observed minus calculated, is at the bottom. Background has been subtracted prior to plotting.

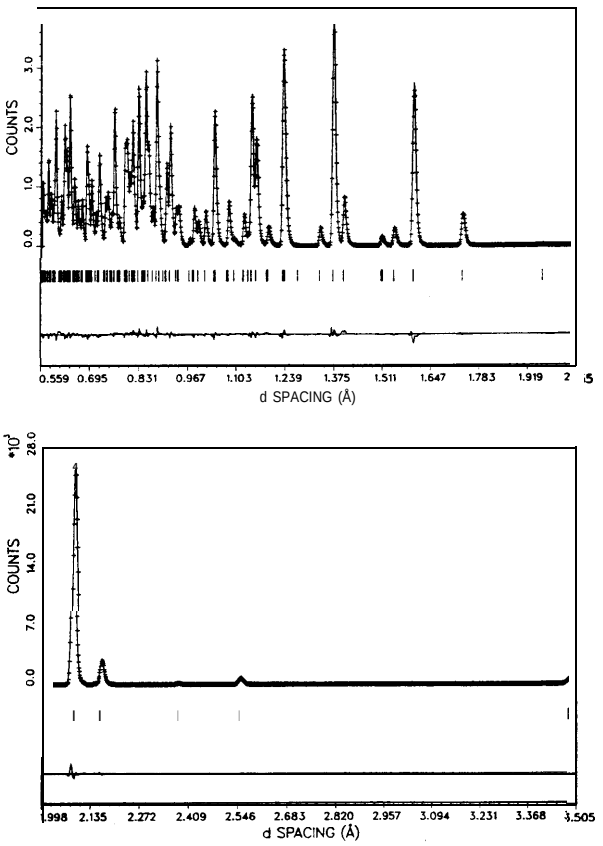

Fig. 8. Raw data (+) and calculated diffraction profile (solid line) from Rietveld refinement of $A1_20_3$ data collected on the 90° detector group of the SEPD. Format same as Fig. 7.

general, however, these errors appear to be not much larger than one standard deviation.

The precision achieved for the refined values of the atom positions and temperature factors improves both with resolution and with the extension of the data set into the small-d-spacing region that is achieved in back scattering. For the case of atom positions, the standard deviations appear to scale roughly with resolution. However, for the case of anisotropic temperature factors, the extension of the data set into the small-d-spacing region appears to have the dominant effect. Thus, the standard deviations for the U_{ij}'s for the same scattering angle of the SEPD and GPPD are almost identical, while a difference of nearly a factor of two is seen when comparing the 150 and 90° refinements for the same instrument. This result illustrates the importance of small-d-spacing data for the accurate determination of temperature factors. As has been demonstrated previously, pulsed neutron source diffractometers are particularly well suited for data collection at small *d* spacings because of the large neutron ***flux*** combined with a short pulse length at short wavelengths. Of course, this advantage can only be exploited for samples where the signal-to-noise ratio and resolution in the small-d-spacing region are sufficient to allow reliable refinements.

Several improvements in data analysis can also be identified. Since instruments can collect data at many different scattering angles simultaneously, Rietveld analysis codes have been developed which will simultaneously refine data from more than one scattering angle (Larson & Von Dreele, 1988). The back-scattering data provide high resolution extending to small *d* spacings while the lower-angle data contain the larger-d-spacing reflections. For an instrument optimized for multiple-angle data analysis, the repetition rate could be several times larger than that used on the GPPD and SEPD because a smaller wavelength range (λ_{min}-λ_{max}) would be required, assuming that such an increase in repetition rate would not compromise the quality of data acquired on other instruments utilizing the pulsed source. Simple choppers could be used to eliminate frame overlap. The combined data set from the multiple angles would cover a large d-spacing range with a composite resolution curve which could be roughly optimized for a given structural problem. The overall data rate would be increased several fold.

One of the problems in data analysis which has been encountered in the initial operation of the SEPD and GPPD involves the accurate characterization of the incident spectrum and the method of passing this information to the Rietveld analysis computer code. The analytical function described by Von Dreele, Jorgensen & Windsor (1982) may not accurately model the effective incident spectrum in all cases. For an electronically focused diffractometer, the effective incident spectrum is actually a spectrum which, for any time channel, has been averaged over a range of wavelengths by the focusing operation. Features which are sharp in the transmitted-beam spectrum, e.g. Bragg cutoffs due to window materials in the incident beam, are smoothed by the focusing. Nevertheless, the effective incident spectrum is not always adequately modeled by a monotonic function, especially when heat shields or thick sample-environment containers, such as pressure cells, are used at the sample position.

Another systematic error is caused by delayed neutrons. For a uranium target, where some fissions are produced, a constant background of delayed neutrons is present for both sample and incident-spectrum data. These delayed neutrons have nearly the same energy spectrum as the prompt neutrons, but exhibit an essentially time-independent flux on the time scale of the repetition rate of the source. In a Rietveld refinement, this contribution to the background can be adequately handled by including a constant background term that is not multiplied by the incident spectrum (Rotella, 1988). In an incident-spectrum determination, the constant background from delayed neutrons can be determined correctly by fitting to an analytical function only if the other terms of the function accurately model the time-dependent spectrum. Such is not the case for the presently used function (Von Dreele, Jorgensen & Windsor, 1982). Fortunately, these errors are small for present instruments. However, future attempts to improve data analysis should address these problems.

Concluding remarks

The GPPD and SEPD at IPNS have nicely demonstrated the electronic time-focusing technique which allows large detector groups in a TOF powder diffractometer to be used at any scattering angle. This focusing technique also eliminates the constraint of using a diffractometer only on the incident flight path for which it is designed. The initial operation of these instruments has allowed the identification of some improvements which could be considered for future designs. For example, the use of position-sensitive detectors at the forward scattering angles combined with electronic focusing in two dimensions would allow even larger detector areas and would result in a more nearly Gaussian geometrical resolution function and higher resolution at the small scattering angles. Higher overall data rates will, of course, require the use of faster microcomputers to perform the focusing calculations. Improvements are needed in the measurement and parameterization of the incident neutron spectrum versus wavelength and the peak shape versus wavelength in order to achieve the full potential of the Rietveld structural refinement technique for pulsed-source data which cover a large

range of ***d*** spacings. These and other new developments will undoubtedly be realized in the near future.

The authors wish to acknowledge the help of numerous ANL staff who have assisted with the engineering, fabrication, installation and maintenance of these instruments. This work has been supported by the US Department of Energy, BES-Materials Sciences, under Contract W-3l-109-Eng-38.

References

ANDRESEN, A. F. & SABINE, T. M. (1977). *J. Appl. Cryst.* 10, 479-501.

BROWN, B. S., CARPENTER, J. M., JORGENSEN, J. D., PRICE, D. L. & KAMITAKAHARA, W. (1982). In Novel *Materials and Techniques in Condensed Matter,* edited by G. W. CRABTREE & P. VASHISHTA, pp. 311-340. New York: North-Holland.

BURAS, B., LECIEJEWICZ, J., NITE, W., SOSNOWSKA, I., SOSNOWSKA, J. & SHAPIRO, F. (1964). *Nucleonika, 9, 523-538.*

CARPENTER, J. M. (1967). *Nucl. Instrum. Methods, 47,* 179-180.

CARPENTER, J. M. (1977). *Nucl. Instrum. Methods, 145, 91-113.*

CARPENTER, J. M., BLEWITT, T. H., PRICE, D. L. & WERNER, S. A. (1979). *Physics Today,* December, pp. 42-49.

CARPENTER, J. M., PRICE, D. L. & SWANSON, N. J. (1978). *IPNS - A National Facility for Condensed Matter Research.* Report No. ANL-78-88. Argonne National Laboratory, Argonne, IL, USA.

CRAWFORD, R. K., DALY, R. T., HAUMANN, J. R., HITTERMAN, R. L., MORGAN, C. B., OSTROWSKI, G. E. & WORLTON, T. G. (1981). IEEE *Trans. Nucl. Sci. NS-28, 3692-3700.*

FABER, J. JR (1984). *Rev. Phys. Appl. 19, 643-647.*

FABER, J. JR & HITTERMAN, R. L. (1986). In *Advances in X-ray Analysis,* Vol. 29, edited by C. S. BARRETT, J. B. COHEN, J. FABER JR, R. JENKINS, D. E. LEYDEN, J. C. Russ & P. K. PREDECKI, pp. 119-130. New York: Plenum Press.

GRAHAM, K. F. & CARPENTER, J. M. (1972). *Nucl. Sci. Eng. 49, 418-437.*

HAUMANN, J. R., DALY, R. T., WORLTON, T. G. & CRAWFORD, R. K. (1982). *IEEE Trans. Nucl. Sci. NS-29, 62-66.*

HEWAT, A. W. & BAILEY, I. (1976). Nucl. *Instrum. Methods, 137, 463-471.*

IKEDA, S. & CARPENTER, J. M. (1985). Nuc1. *Instrum. Methods, A239, 536-544.*

JORGENSEN, J. D. (1988). In *Chemical Crystallography with Pulsed Neutrons and Synchrotrons Radiation,* edited by M. A. CARRONDO & G. A. JEFFREY, pp. 159-186. NATO Advanced Study Institute Series. Reidel: Kluwer Academic Publishers.

JORGENSEN, J. D. & FABER, J. JR (1983). In *Proceedings of the Sixth Meeting of the International Collaboration on Advanced Neutron Sources,* pp. 105-114. Report No. ANL-82-80. Argonne National Laboratory, Argonne, IL, USA.

JORGENSEN, J. D.& ROTELLA, F. J. (1982). *J. Appl Cryst. 15, 27-34.*

JORGENSEN, J. D. & WORLTON, T. G. (1985). *J. Chem. Phys. 83, 329-333.*

LARSON, A. C. & VON DREELE, R. B. (1988). *Generalized Structure Analysis System.* Report No. LAUR86-748. Los Alamos National Laboratory, Los Alamos, NM, USA.

ROTELLA, F. J. (1988). *User Manual for Rietveld Analysis of Time-of-Flight Neutron Powder Diffraction Data at IPNS.* Argonne National Laboratory, Argonne, IL, USA.

TOMPSON, C. W., MILDNER, D. F. R., MEHREGANY, M., SUDOL, J., BERLINER, R. & YELON, W. B. (1984). *J. Appl. Cryst.* 17, 385-394.

VON DREELE, R. B., JORGENSEN, J. D. & WINDSOR, C. G. (1982). *J. App. Cryst. 15,* 581-589.

WINDSOR, C. G. (1981). *Pulsed Neutron Scattering. New* York: Wiley.